IAC-24,C2,IPB,21,x87780

SHM of space structures: use of polarization-maintaining fibers to decouple the thermo-mechanical effect on Fiber Bragg Grating sensor measurements

Emanuele Casciaro[a]*, Tanya Scalia[b], Marta Albano[c], Paolo Bettini[d]

[a] *Department of Aerospace Science and Technology, Politecnico di Milano, Via La Masa 34, 20156, Milan, Italy,* emanuele.casciaro@polimi.it
[b] *Engineering & Technology Directorate, via del Politecnico snc 00133 Rome, Italy*, tanya.scalia@asi.it
[c] *Engineering & Technology Directorate, via del Politecnico snc 00133 Rome, Italy*, marta.albano@asi.it
[d] *Department of Aerospace Science and Technology, Politecnico di Milano, Via La Masa 34, 20156, Milan, Italy,* paolo.bettini@polimi.it
* Corresponding Author

Abstract

Fiber Bragg Grating (FBG) sensors have gained prominence in space applications due to their lightweight, compact design, and immunity to electromagnetic interference. This is a crucial advantage in space environments, where electromagnetic radiation from different sources can disrupt electronic sensors. Their utility in monitoring temperature and strain in harsh environments is fundamental in order to ensure the integrity and safety of critical space components. Furthermore, the potential for mass production of FBG sensors makes them cost-effective for large-scale space missions, facilitating the integration of multiple sensors. The operating principle of FBG sensors is based on the interaction of light with a periodic variation of the refractive index of an optical fiber. Changes in the physical parameters of this grating are reflected in the optical signal. Thermal and mechanical stimuli produce similar effects. To distinguish these contributions, the present research aims to exploit intrinsic decoupling methodologies. This involves utilizing FBG sensors inscribed within birefringent or polarization-maintaining (PM) optical fibers. These fibers exhibit unique refractive index distributions across their cross-section, creating dual principal axes along which light propagates at different velocities. This characteristic generates two discrete peaks from a single sensor, each responding differently to strain and temperature variations. Leveraging this property allows for effective decoupling of localized thermo-mechanical measurements using only the fiber itself. Previous studies have confirmed the feasibility of this approach, yielding promising results. In this work, we aimed to improve the experimental results by making the resolution matrix of the Bragg equation system well-conditioned. To achieve this, we considered not the two equations corresponding to the two reflected peaks but rather the wavelength of one peak and the difference in wavelengths between the two peaks. An analytical model was developed to evaluate the system resolution matrix, providing the wavelength variation of the two peaks caused by changes in temperature and strain. This confirmed the validity of the strategy and guided the development of a dedicated set-up. This set-up enables the verification of the behavior of birefringent fibers under purely thermal effects, purely mechanical effects, and simultaneous exposure to both. Panda polarization-maintaining (PM) optical fibers have been calibrated and tested, achieving a thermo-mechanical decoupling with an accuracy and precision of -1.65 ± 3.1 ℃ for temperature and 58.28 ± 56.2 $\mu\varepsilon$ for mechanical strain. Future work will investigate the behavior of the fiber embedded within a composite component, with different orientations of the polarization axes.

Keywords: Fiber Bragg grating sensors, Polarization-maintaining fiber, Birefringent fiber, Thermo-mechanical decoupling, Composite materials, Structural Health Monitoring.

Nomenclature

λ_b	Bragg wavelength.
n_{eff}	Effective refractive index.
Λ	Nominal period of the refractive index modulation.
$\Delta\lambda_b$	Bragg wavelength variations.
K_T	Temperature sensitivity.
K_ε	Strain sensitivity.
ΔT	Temperature variations.
$\Delta\varepsilon$	Strain variations.
F	Tensile force.
μ	Friction coefficient.
θ	Angle subtended by the fiber segment, assuming it is positioned on a circumference.
λ_{fast}	Wavelength of the fast peak.
λ_{slow}	Wavelength of the slow peak.
$d\lambda$	Difference between the wavelengths of the slow peak and the fast peak.
n	Refractive index.
a_0	Coefficient of the polynomial proposed by C.Z. Tan and J. Arndt.
a_1	Coefficient of the polynomial proposed by C.Z. Tan and J. Arndt.

a_2	Coefficient of the polynomial proposed by C.Z. Tan and J. Arndt.
a_3	Coefficient of the polynomial proposed by C.Z. Tan and J. Arndt.
a_4	Coefficient of the polynomial proposed by C.Z. Tan and J. Arndt.
λ_0	Initial wavelength.
$\Delta\beta_{ij}$	Variation of relative dielectric impermeability tensor.
π_{ijkl}	Fourth-order tensor relating the variation of the relative dielectric impermeability tensor to the stress state.
σ_{kl}	Stress tensor.
p_{ijrs}	Fourth-order tensor relating the variation of the relative dielectric impermeability tensor to the strain tensor.
ε_{rs}	Strain tensor.
p_{12}	Cross photo-elastic coefficient.
α_T	Coefficient of thermal expansion.
B	Birefringence.
C	Stress-optic coefficient.
E	Young's modulus.
ν	Poisson coefficient.
$\Delta\alpha$	Difference between the coefficient of thermal expansion of cladding and stress rods.
a	Geometrical parameters.
b	Geometrical parameters.
F_m	Force acting per unit length perpendicular to the fiber axis.
p_{11}	Photo-elastic coefficient.
d	Fiber diameter.
F_{axial}	Force parallel to the fiber axis.
$T_{setting}$	Characteristic temperature of the manufacturing process for birefringent fibers.
T_{amb}	Ambient temperature.
S_1	Generic output signal number 1.
S_2	Generic output signal number 2.
c	Generic component of a matrix.
d	Generic component of a matrix.
e	Generic component of a matrix.
f	Generic component of a matrix.
D	Determinant of a matrix.
E_d	Parameter to quantify how the effects of strain and temperature are uncoupled.
K	Condition number of the matrix.

Acronyms/Abbreviations

FBG	Fiber Bragg Grating.
PM	Polarization-maintaining.
SHM	Structural Health Monitoring.
LPG	Long Period Grating.
SMF	Single-Mode Fiber.
DTG	Draw Tower Gratings.
SEM	Scanning Electron Microscope.
ABS	Acrylonitrile Butadiene Styrene.
EPS	Sintered Expanded Polystyrene.
XPS	Extruded Polystyrene.
IR	Infrared.
CTE	Coefficient of thermal expansion.

1. Introduction

Optical fibers are utilized across various fields, from telecommunications to sensing technologies. The optical medium that carries information, combined with the high propagation speed of signals and the reduced size, makes them advantageous compared to sensors currently employed. However, their widespread adoption is hindered by their fragility and the complexity of the physical phenomena governing their operation. In the aerospace sector, optical fibers are being studied as a Structural Health Monitoring (SHM) system for assessing structural integrity.

Optical fibers are made from glass or plastic and are used to transmit light signals over long distances. They consist of three main layers: core, cladding, and protective coating. Light signals are injected into the fiber at one end. Due to the total internal reflection at the core-cladding interface, these light signals are guided through the core with minimal attenuation.

In optical fibers, sensors such as Fiber Bragg Gratings (FBGs) can be inscribed. These are a type of distributed Bragg reflectors that reflect specific wavelengths of light while transmitting others. FBGs are created by exposing the fiber core to a periodic pattern of ultraviolet light, which induces a periodic modulation of the refractive index within the core. This modulation results in the reflection of particular wavelengths, known as the Bragg wavelength, which is determined by the grating period and the effective refractive index of the core. This relationship is described by Equation 1 [1]:

$$\lambda_b = 2\, n_{eff}\, \Lambda. \qquad (1)$$

Tracking this wavelength peak is the sensing principle of the FBG sensor, providing an indirect measurement of strain and/or temperature in the structure. Axial strain on the fiber and temperature variations affect both the effective refractive index and the grating period, thereby altering the reflected wavelength. The relationship that links temperature and strain to the variation in Bragg wavelength is expressed by Equation 2 [1]:

$$\Delta\lambda_b = \lambda_b(K_T\, \Delta T + K_\varepsilon\, \Delta\varepsilon). \qquad (2)$$

FBG sensors are highly regarded due to their lightweight design, compact size, embeddability in composite materials, and resistance to electromagnetic interference. Thermo-mechanical decoupling represents one of the major challenges of this technology, as both

temperature and strain produce the same effect on wavelength variation.

Various solutions have been proposed to address this issue. The simplest approach involves the use of two closely positioned FBG sensors, with one being unaffected by mechanical strain. This technique entails the insertion of a capillary tube to isolate one of the sensors [2], [3]. While this method is widely used, it is highly invasive. Moreover, the optical fibre needs to be cut to introduce the sleeve, which makes the possibility of having several gratings in the same fibre optic quite difficult.

New techniques and sensors have been developed for multi-parameter measurement (strain and temperature), such as dual gratings at the same location using a standard FBG and a Long Period Grating (LPG) [4], [5], chirped FBG and Fabry-Perot [6], different FBG sensor diameters [7] and FBG with a thermochromic material [8]. Qazi et al. [9] have obtained promising results with a configuration involving a D-shaped cross-sectional area of the fiber. G. Pereira et al. [10] used two FBG sensors in polymeric tensile tests, positioning them at the same location on the specimen but oriented differently with respect to the load direction.

Birefringence has also been studied as a potential decoupling technique. A. K. Singh et al. [11] proposed an innovative approach using a standard optical fiber (SMF) embedded in a composite laminate to induce birefringence. The parameters investigated included the Bragg wavelength and the sensor bandwidth. The errors for strain and temperature measurements were found to be 62 $\mu\varepsilon$ and 1.94 ℃, respectively.

Birefringent optical fibers have undergone extensive examination to assess their effectiveness as sensors in various setups, including local and integral measurement systems. Sagnac interferometer yielded impressive results in terms of decoupling [12]. This study utilizes segments of birefringent fibers, joined with appropriately phased principal polarization axes. It was possible to achieve accurate measurements with relative errors of approximately $\pm 3\ \mu\varepsilon$ and ± 0.4 ℃. In another study, Zhou et al. [13] employed a FBG connected in series to a segment of birefringent optical fiber, reporting measurement errors of 1 ℃ and 21 $\mu\varepsilon$. The work of Ferreira et al. [14] explored the use of Bow-tie birefringent fibers to distinguish signals from slow and fast axes. The article focuses on describing the results obtained with errors of approximately ± 1.3 ℃ and $\pm 13.5\ \mu\varepsilon$. Cross-tests were also performed and have yielded promising results. Lastly, Zhang et al. [15] presented an integral measurement system utilizing a distributed sensor on birefringent fiber for measuring pressure along its entire length. The system demonstrated accurate decoupling of pressure and temperature with an accuracy of 0.014 ℃ and 0.15 bar.

Numerical investigation by Andrea Annunziato et al. simulated the presence of birefringent optical fibers embedded in a composite material [16]. They found variations in temperature sensitivity due to different fibers and embedding techniques. Bow-Tie fiber demonstrated the best performance in decoupling strain and temperature.

The work of J. Van Roosbroeck et al. [17] explored the use of a Bragg grating sensor inscribed in a PM fiber. Thermo-mechanical decoupling was verified, employing the difference between the two peaks for temperature measurements and the wavelengths of the sensors for strain measurements.

However, these techniques require advanced and costly technology, skilled operators, and in some cases, are not commercially available. Moreover, all these strategies have been studied in laboratory settings and function effectively only in controlled environments, free from environmental disturbances.

In this article, a simple approach, similar to that proposed by J. Van Roosbroeck, is presented for multi-parameter measurement, where strain and temperature can be measured independently using commercially available technology. The objective is to develop a robust sensor for strain and temperature measurement, capable of functioning reliably in industrial environments.

For this reason, this study address the challenge of decoupling thermo-mechanical measurements using optical fiber Bragg grating (FBG) inscribed in birefringent optical fibers. These fibers exhibit two polarization axes, resulting in two sensor peaks at different wavelengths that respond differently to thermal and mechanical changes. The method involves monitoring the evolution of the peak wavelengths after performing the calibration of the sensors. The advantage of this technique lies in its ability to decouple thermal measurements from mechanical ones at the same measurement point without the need for additional components.

This research builds on the work presented in [18] and aims to improve its outcomes. The first phase of the research focused on enhancing the experimental setup. A dedicated test bench was constructed to assess the optical fiber by applying only mechanical stress, varying the temperature, or applying both types of stimuli simultaneously. Previous tests did not allow for the accurate assessment of force and displacement due to measurement hysteresis. The setup was improved by minimizing any contributions that could affect sensor measurements.

A different strategy for decoupling thermal effects from mechanical ones was also considered, i.e., tracking the variation of a wavelength and the difference between the two wavelengths of the peaks. A numerical model was developed to evaluate the influence of temperature and strain on the wavelength shift of the peaks.

The paper is structured as follows: Section 2 describes the experimental setup and the fibers used. Section 3 outlines the equations developed in the numerical model. Section 4 presents the numerical and experimental results, while Section 5 discusses these findings. Section 6 addresses the conclusions and future developments.

2. Materials and methods

The optical fibers used in the experimental campaign are Panda polarization-maintaining fibers (Figure 1). They have a cladding diameter of 125 μm and are coated with Ormocer. FBG sensors with a length of 8 mm are inscribed using Draw Tower Gratings (DTG) technology.

The DTG process is a highly efficient and precise technique for manufacturing optical fibers with embedded FBGs. It enhances their performance in sensing applications by integrating the FBGs directly into the fiber drawing process. The draw tower is a vertical production system where optical fibers are manufactured by heating and drawing a glass preform into a fine fiber. This is a high-precision process occurring in a controlled environment. The key aspect of the DTG process is that the FBGs are inscribed directly into the fiber during its drawing, as opposed to a post-fabrication inscription that occurs in traditional methods.

The rod elements, inducing the stress state, are essential for inducing birefringence and obtaining the two polarization axes. The diameter of the rods are approximately 31.35 μm, while the distance of the center of the rods from the center of the core is about 18.625 μm. These values were calculated for the fibers used in this work using SEM technology.

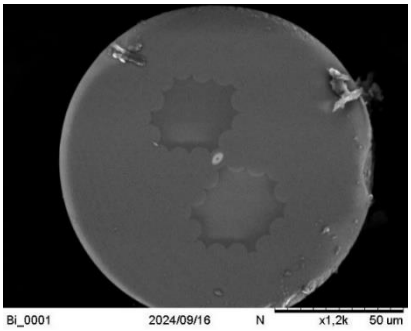

Fig. 1. SEM cross-section of PM Panda fibers used in this work.

The small dimensions of the optical fibers used, along with the mechanical and thermal stimuli, require a dedicated experimental setup. Therefore, a test bench was developed as described in the work [18], shown in Figure 2.

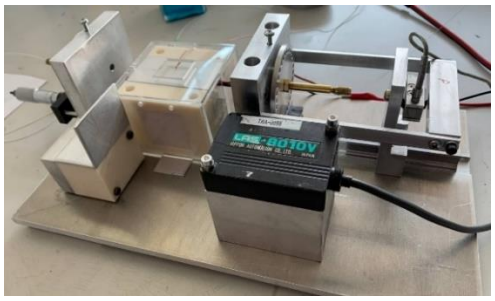

Fig. 2. Experimental setup used in previous experimental campaign.

The operation of the test bench involves securing the fiber between two chucks to prevent rotation and translation. A manually controlled micrometric slide enables fiber deformation by moving one of the chucks. The deformation is visualized using a graduated scale on the micro-slide.

The sensor is positioned at the center of the thermal chamber, which is enclosed by plexiglass, with the temperature controlled by a heating element. This setup enables temperature variation around the sensor, which is isolated from the external environment. A thermocouple is positioned near the sensor to record the temperature experienced by the sensor.

The apparatus includes a load cell to measure the load on the fiber and a laser displacement sensor to assess deformation. During loading and unloading cycles, a hysteretic behavior was observed, preventing the effective use of data obtained from the load cell and the displacement sensor.

In this study, the experimental setup was modified (Figure 3).

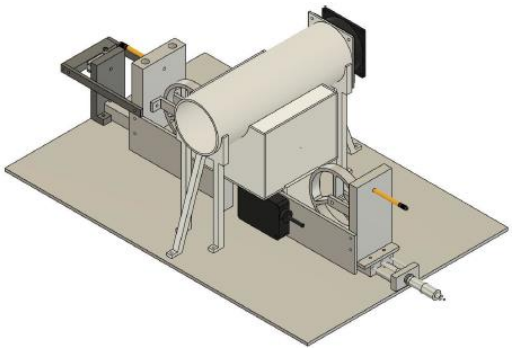

Fig. 3. Modified experimental setup to enhance its effectiveness and expand usable temperature range.

As can be observed, the stresses are applied in the same manner as in the previous version. The changes made focus on improving the precision and accuracy of the applied stresses, expanding the usable temperature range for testing and enhancing the safety of securing the fiber to the test bench. The thermal chamber has been modified to increase the effectiveness of its insulation.

An ABS (Acrylonitrile Butadiene Styrene) support has been added to insulate the chamber on the test bench. Three materials were considered for the thermal chamber walls: EPS (Sintered Expanded Polystyrene), XPS (Extruded Polystyrene), and fine glass fibers.

Table 1. Theoretical temperature calculated inside thermal chamber as a function of wall materials.

	T_{max} [℃]	T_{min} [℃]
EPS	86	-38
XPS	85	-38
Fine glass fibers	82	-35

The values were obtained by evaluating the temperatures using MATLAB and Simulink. The final choice was fine glass fibers. Although the temperature range appears smaller, the temperatures reached are well within the material limits (-195 ℃ and 230 ℃). In contrast, EPS and XPS are at risk of damage from high temperatures.

Figure 4 illustrates the thermal cycle obtained, considering 2 minutes as the period for temperature stabilization. The full range of achievable temperatures has been evaluated.

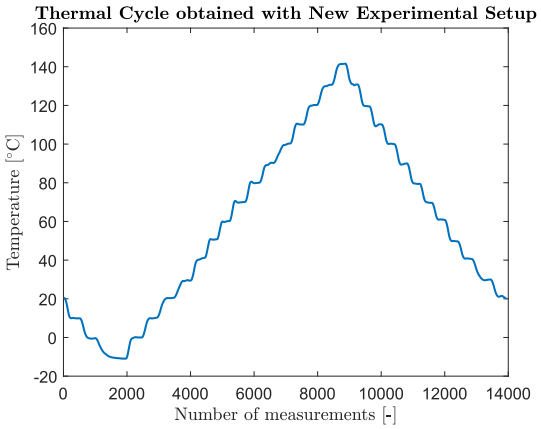

Fig. 4. Thermal cycle obtained with new experimental setup, considering 2 minutes for temperature stabilization.

The thermal chamber is heated by a Peltier cell and a heating element located above the chamber (Figure 5). Both devices are connected to a radiator.

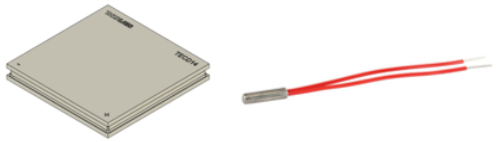

Fig. 5. Peltier cell and electric heater to increase temperature of thermal chamber.

The radiator is located within a duct, and cooling occurs through forced convection. Airflow is provided by a fan positioned at the end of the duct.

Fiber clamping is ensured by two chucks at the ends of the test bench.

Fig. 6. Optical fiber clamping system (chuck) and pulley for reducing the force applied to chucks during fiber deformation.

During tests with the previous setup, some fibers broke during mechanical cycling. This was due to the use of old chucks, which have been replaced with Newport chucks, model FPH-S-2.5 (Figure 6).

To prevent the instrumentation from applying excessive load on the fiber during the deformation phase, two pulleys were added, onto which the fiber is positioned immediately after leaving the chucks. This configuration ensures that only 10% of the force applied to the fiber at the sensor region is transmitted to the chucks, which were the primary cause of fiber breakage. The formula employed for the design of these elements is the Euler–Eytelwein [19]:

$$F = F_0 e^{\mu\theta} \qquad (3)$$

considering a segment of fiber where F and F_0 are the tension forces at the two ends.

Each component of the setup was designed using Autodesk. Simulations were conducted to assess the deformation of each element during mechanical cycling.

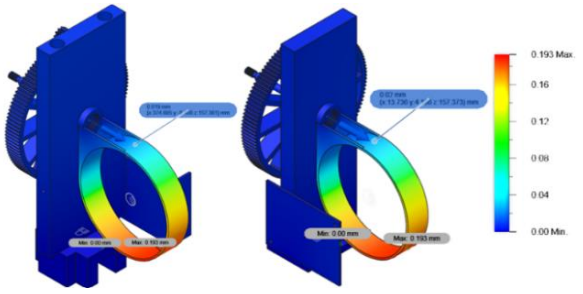

Fig. 7. Numerical analysis of deformations in instrumentation elements during loading and unloading cycles of fiber. On the left, aluminum component, and on the right, steel component.

These simulations (Figure 7) highlighted the influence of component deformation on the measurement of optical fiber strain. To minimize the impact of the

components, some elements were made from steel, such as the load-reducing pulleys. This ensures that the deformation measured by the test bench accurately reflects the strain experienced by the fiber, as the deformation of other components is negligible.

The final test bench addresses the issues encountered with the previous setup. The hysteresis caused by the components was solved by replacing the chucks, which previously enabled fibers sliding during deformation (Figure 8 and Figure 9).

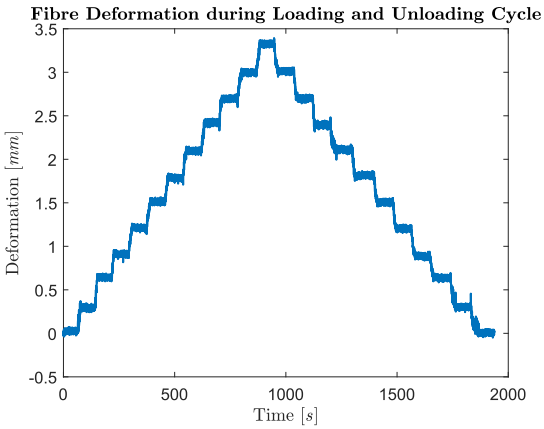

Fig. 8. Loading and unloading cycle of optical fiber with deformation from 0 mm to 3.5 mm.

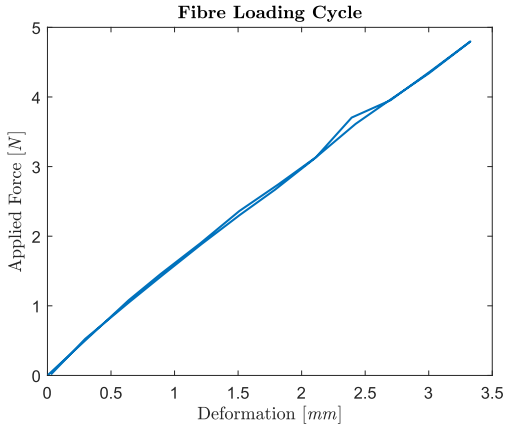

Fig. 9. Loading and unloading cycle of optical fiber considering force detected by load cell and deformation measured by laser sensor.

The entire setup is connected to a computer running a virtual instrument with NI LabVIEW, enabling control of the instrumentation. This setup allows for real-time monitoring of the temperature measured by the thermocouple, the force on the fiber via the load cell (LRF400 from Futek Advanced Sensor Technology, Inc.), and the displacement measured by the laser sensor (LAS-8010 from Hana Tech.). Additionally, the Micron Optics software provides the capability to visualize the wavelength variations of the two peaks. During testing, the optical fiber is connected to a polarization controller (Figure 10) consisting of quarter-wave and half-wave plates, enabling precise phase shifts to control light polarization and, consequently, the intensity of the two peaks.

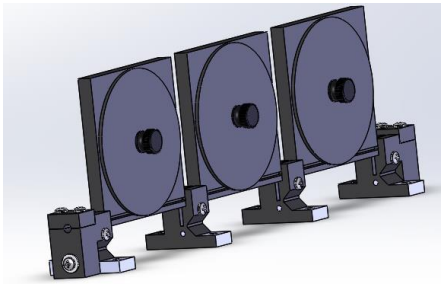

Fig. 10. Polarization controller required to modify resonance peaks of FBG sensor.

3. Theory and calculation

To identify the thermal and mechanical effects, it is necessary to work with the representative matrix of the sensor inscribed in the optical fiber. Considering a PM optical fiber, two polarization axes along which light propagates can be defined: the slow axis and the fast axis. This is due to the different distribution of the refractive index in the cross-section of the fiber and along its length. Consequently, two resonance peaks of the FBG sensor (slow and fast) can be identified along these respective axes. In this way, two equations with two unknowns can be derived by tracking the variations in the wavelengths of the peaks, which represent the sensor response to thermal and mechanical stimuli (Equations 4). As in other studies, cross-sensitivities have been considered negligible [5].

$$\begin{pmatrix}\Delta\lambda_{fast}\\ \Delta\lambda_{slow}\end{pmatrix}=\begin{bmatrix}K_{\varepsilon}^{fast} & K_{T}^{fast}\\ K_{\varepsilon}^{slow} & K_{T}^{slow}\end{bmatrix}\begin{pmatrix}\Delta\varepsilon\\ \Delta T\end{pmatrix}. \qquad (4)$$

This approach does not enable the development of a high-performance sensor. This limitation is due to the ill-conditioned nature of the resulting matrix. The strategy proposed in this work involves using one equation related to a single peak and, as the second equation, the difference between the two peaks (Equations 5).

$$\begin{pmatrix}\Delta\lambda_{fast}\\ \Delta\, d\lambda\end{pmatrix}=\begin{bmatrix}K_{\varepsilon}^{fast} & K_{T}^{fast}\\ K_{\varepsilon}^{d} & K_{T}^{d}\end{bmatrix}\begin{pmatrix}\Delta\varepsilon\\ \Delta T\end{pmatrix}. \qquad (5)$$

This choice is based on the behavior of the difference between the two peaks. As observed in the previous work [18], increasing the temperature causes the difference to decrease, while increasing the strain causes the difference to increase. This approach enables to obtain a negative value for temperature sensitivity. Consequently, the

resulting matrix should be well-conditioned, overcoming the issues of the previous approach.

To verify the feasibility of this strategy, a generic theoretical model was developed without characterizing the birefringent fibers. The variations in the wavelengths of the two peaks due to thermal and mechanical stimuli were evaluated. This enabled the determination of the conditioning degree of the representative matrix of the FBG sensor and validated this strategy.

To develop the model, we start from Equation 1 and evaluate the effects of temperature and strain on the refractive index and on the grating pitch of the sensor.

The temperature dependence of the refractive index can be associated with various properties and physical processes in materials, such as thermal lensing, light scattering, phase transitions in transparent dielectrics, density, and mean polarizability. To estimate the variation of the refractive index with temperature for SiO_2 fibers, the model proposed by C.Z. Tan and J. Arndt [20] was utilized. This model is valid in the infrared (IR) wavelength region ($1.44 < \lambda < 4.77\ \mu m$) at temperatures ranging from 23.5 ℃ to 481 ℃. In their work, they considered Equation 6:

$$n^2 - 1 = a_0(T) + \frac{a_1(T)}{\lambda^2} + \frac{a_2(T)}{\lambda^4} + \frac{a_3(T)}{\lambda^6} + \frac{a_4(T)\,\lambda^2}{\lambda^2 - \lambda_0^2}. \quad (6)$$

An increase in temperature will lead to an increase in the refractive index for all the wavelengths considered.

The change in the refractive index caused by stress is known as the photo-elastic effect. As discussed in [21], the refractive index of a crystal is determined by the indicatrix, an ellipsoid whose coefficients are the components of the relative dielectric impermeability tensor β_{ij}. Therefore, the small change in the refractive index due to stress is, more precisely, a change in the shape, size, and orientation of the indicatrix. From the small changes in the coefficients β_{ij}, it is possible to derive the variation in the refractive indices.

$$\Delta\beta_{ij} = \pi_{ijkl}\sigma_{kl}\,. \quad (7)$$

The photo-elastic effect is sometimes expressed in terms of the strains. Hence, Equation 7 may be alternatively written as

$$\Delta\beta_{ij} = p_{ijrs}\varepsilon_{rs}\,. \quad (8)$$

Consider direction 1 as the fiber axis, with directions 2 and 3 orthogonal to both the fiber axis and each other. In the case of an isotropic material subjected to uniaxial loading, the change in the refractive index along the three principal axes can be defined as follows:

$$\begin{aligned}\Delta n_1 &= -\frac{1}{2}n_1^3\,\Delta\beta_1 = -\frac{1}{2}n_1^3\,\pi_{11}\,\sigma = -\frac{1}{2}n_1^3\,p_{11}\,\varepsilon\\ \Delta n_2 &= -\frac{1}{2}n_2^3\,\Delta\beta_2 = -\frac{1}{2}n_2^3\,\pi_{12}\,\sigma = -\frac{1}{2}n_2^3\,p_{12}\,\varepsilon\\ \Delta n_3 &= -\frac{1}{2}n_3^3\,\Delta\beta_3 = -\frac{1}{2}n_3^3\,\pi_{12}\,\sigma = -\frac{1}{2}n_3^3\,p_{12}\,\varepsilon\,.\end{aligned} \quad (9)$$

In case of a traditional fiber optic, the light will propagate along the fiber direction 2 and 3 with the same velocity and, hence, with the same refractive index. Then the change in the refractive index can be generally written as

$$\Delta n = -\frac{1}{2}n^3 p_{12}\,\varepsilon\,. \quad (10)$$

From this equation, it can be observed that in the case of elongation, since both p_{12} and n are positive, the refractive index will decrease. The assumption of considering a standard fiber for the variation of the refractive index with strain is necessary to achieve a simple model.

When considering a birefringent fiber, the matrix does not have all off-diagonal terms equal, but these values are not available in the literature. Moreover, by applying the same cross photo-elastic coefficient (p_{12}) to both polarization axes, it is implicitly considered the worst-case scenario. In fact, a different cross photo-elastic coefficient would only increase the differences between the signals of the two axes, differentiating their behavior and emphasizing the potential for achieving effective thermo-mechanical decoupling. However, the model remains representative of the fibers considered, as a different coefficient would alter the results without changing the overall behavior of the fiber.

For both strain and temperature, the relationship with the grating pitch is connected to the deformation of the fiber. In the temperature case through the coefficient of thermal expansion (CTE) of the material. The following equations can be derived:

$$\Delta\Lambda = \Lambda\,\varepsilon \quad (11)$$

$$\Delta\Lambda = \Lambda\,\alpha_T\,\Delta T\,. \quad (12)$$

It can be observed that as temperature and strain increase, the grating pitch will also increase and the Bragg wavelength will increase as well.

It is also important to evaluate how birefringence varies as a function of temperature and axial strain. Birefringence is defined as the difference between the refractive indices of the slow axis and the fast axis. From [22], it is known that the general solutions for estimating birefringence as a function of temperature in Panda fibers (Figure 11) is given by Equations 13.

$$B = \frac{C\ E\ \Delta\alpha\ \Delta T}{2(1-\nu)}\left[4\left(\frac{a-b}{a+b}\right)^2 - \frac{3}{4}(a^2-b^2)^2\right]. \quad (13)$$

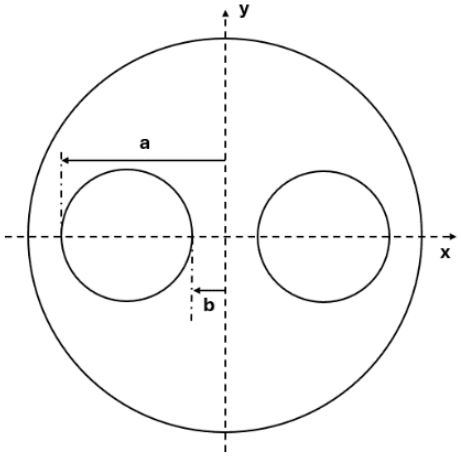

Fig. 11. Parameters for calculation of birefringence in Panda optical fibers.

Finally, we consider the variation in birefringence as a function of axial deformation. Birefringence can be induced in two different ways: intrinsically and extrinsically. The main factors contributing to birefringence include: the presence of an elliptical core, internal mechanical stress on the core or external mechanical stress on the fiber cladding [23]. In the latter case, the cladding transfers mechanical stress to the core due to fiber bending or lateral pressure. In the case of lateral pressure, the induced anisotropy in the fiber results from the photo-elastic effect. If F_m is the force acting per unit length, the birefringence will be [24]:

$$B = \frac{2\ n_{eff}^3\ F_m}{E\ \pi\ d}\ (1+\nu)(p_{11}-p_{12}). \quad (14)$$

In traditional optical fibers, an axial load will not induce birefringence, as the transverse load associated with Poisson effect acts uniformly on the core. However, in PM fibers, such as the Panda and Bow-tie types, the presence of stress rods designed to generate birefringence may lead to sensitivity to axial loading if the Poisson ratio of these stress rods differs from that of the cladding.

By employing Equation 14 and the Poisson coefficients, it is possible to determine the variation in birefringence due to axial load along the fiber (or to axial deformation):

$$\begin{cases} B = \sigma\ \dfrac{2\ n_{eff}^3}{E}\ (1+\nu_{core})(p_{11}-p_{12}) \\ \sigma = \dfrac{4\ F_{axial}}{\pi\ d^2}\left(\nu_{cladding}-\nu_{stressrods}\right) \end{cases}. \quad (15)$$

In terms of axial deformation, Equations 15 can be modified as follows:

$$B = 2\ n_{eff}^3\ \varepsilon\ \left(\nu_{cladding}-\nu_{stressrods}\right)\ (1+\nu_{core})(p_{11}-p_{12}). \quad (16)$$

Considering the model composed of these six equations 6, 10, 11, 12, 13, 16, it is possible to analyze the wavelength shifts of the two peaks in response to a thermal or mechanical stimulus. It is important to emphasize that the model is based on assumptions and simplifications. Nevertheless, it remains a valuable tool for assessing the feasibility of the selected strategy for mechanical-thermal decoupling.

4. Results

4.1 Results of theoretical models

In the numerical model, a fiber with a nominal Bragg wavelength of $1550\ nm$ was considered. Given that SiO_2 has a room temperature refractive index of 1.444, and using Equation 6, the trend reported in Figure 12 was computed.

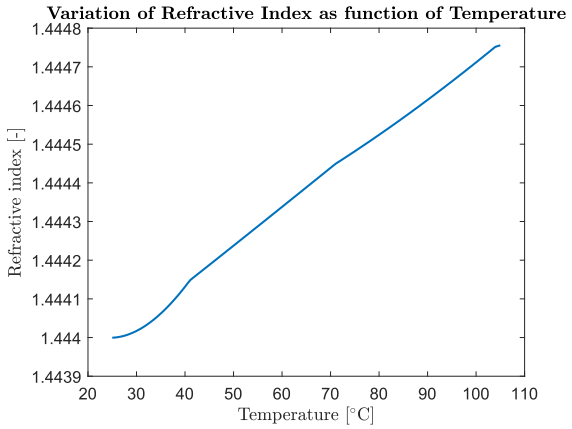

Fig. 12. Variation of refractive index of SiO_2 optical fiber with wavelength of $1550\ nm$ as the temperature changes from 25 ℃ to 105 ℃.

The refractive index increases from a value of 1.44400 to 1.44476 within the temperature range considered, leading to an increase in the Bragg wavelength.

Considering the variation in the refractive index due to strain, Equation 10 and a maximum strain value of 5 % were applied. From [25], it is known that the photo-elastic coefficient of SiO_2 is $p_{12} = 0.27$. The trend of the refractive index is presented in Figure 13.

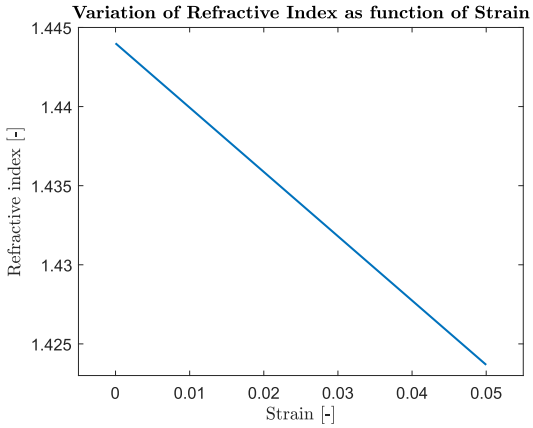

Fig. 13. Variation of refractive index of SiO_2 optical fiber with wavelength of $1550\,nm$ as the strain changes from 0 % to 5 %.

As can be observed from the figure, the refractive index decreases from 1.444 to 1.4237, leading to a reduction in the Bragg wavelength.

Using Equations 11 and 12, it is possible to compute the trends for the grating pitch subjected to changes in temperature and strain (Figure 14 and Figure 15). The data required for this analysis are: grating pitch $\Lambda = 500\,nm$, coefficient of thermal expansion $CTE = 0.8\,(10^{-6})\,℃^{-1}$. For the refractive index, the ranges of interest for temperature and strain are $25\,℃ < T < 105\,℃$ and $0\,\% < \varepsilon < 5\,\%$.

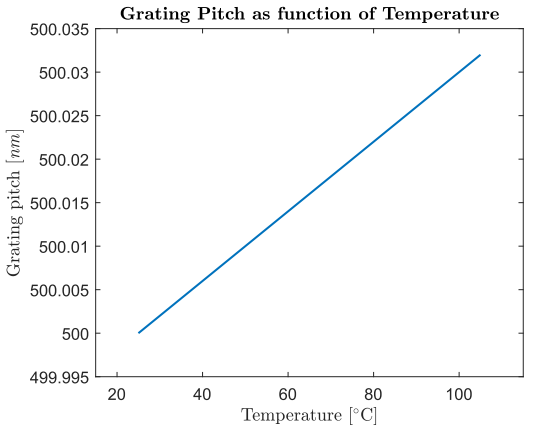

Fig. 14. Variation of grating pitch of FBG sensor with wavelength of $1550\,nm$ as the temperature changes from 25 ℃ to 105 ℃.

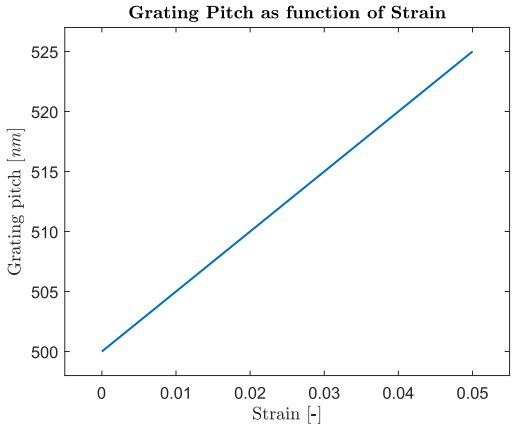

Fig. 15. Variation of grating pitch of FBG sensor with wavelength of $1550\,nm$ as the strain changes from 0 % to 5 %.

A maximum variation of $\Delta\Lambda = 0.03\,nm$ is expected due to temperature changes, and a maximum variation of $\Delta\Lambda = 25\,nm$ within the considered strain range.

Regarding the behavior of birefringence with temperature (Figures 16), the following parameters, taken from [26] and [27], were considered.

Table 2. Characteristic parameters of birefringent optical fibers considered during analysis of birefringence variation as function of temperature.

	Panda	Bow-tie
$C\,[Pa^{-1}]$	$2.43\,(10^{-12})$	$2.43\,(10^{-12})$
$E\,[GPa]$	78	78
$\nu\,[-]$	0.186	0.186
$\Delta\alpha\,[1/℃]$	$0.91\,(10^{-6})$	$0.91\,(10^{-6})$
$T_{setting}\,[℃]$	1000	1000
$a\,[-]$	0.8	0.76
$b\,[-]$	0.16	0.12

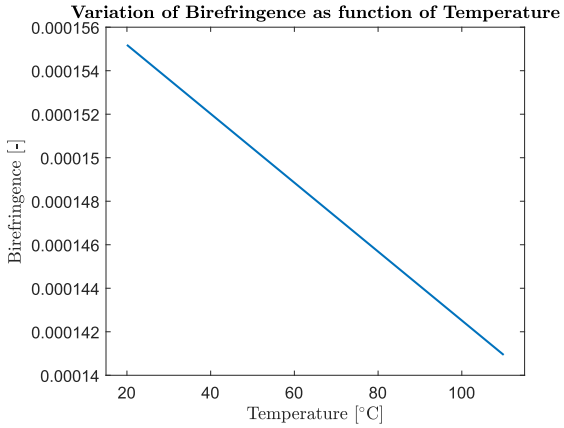

Fig. 16. Variation of fiber optic birefringence as the temperature changes from 20 ℃ to 110 ℃.

$T_{setting}$ is the solidification temperature of the fiber and the onset of birefringence during the manufacturing process. Parameters a and b in the table represent the dimensions shown in Figure 11, but dimensionless with respect to the radius of the fiber. From Figure 16, it is possible to observe that if the temperature increases, the birefringence decreases.

The final property to be analyzed is the birefringence as a function of axial strain (Figure 17). The properties considered for this calculation are listed in the Table 3 for a Panda fiber.

Table 3. Characteristic parameters of birefringent optical fibers considered during analysis of birefringence variation as function of strain.

	Panda
n_{eff} $[-]$	1.444
d $[m]$	0.000125
ν_{core} $[-]$	0.183
$\nu_{cladding}$ $[-]$	0.186
$\nu_{stressrods}$ $[-]$	0.221
p_{11} $[-]$	0.125
p_{12} $[-]$	0.27

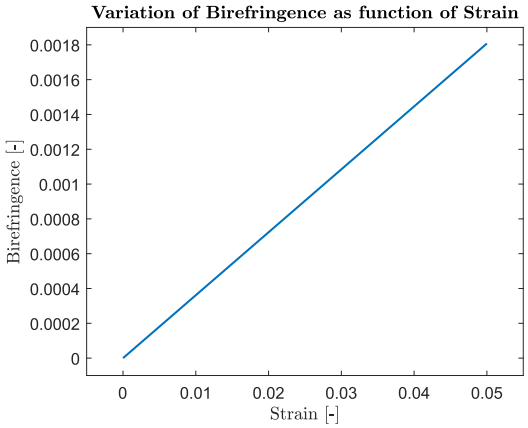

Fig. 17. Variation of fiber optic birefringence as strain changes from 0 % to 5 %.

The birefringence will increase if a tensile load is applied.

With the previously reported data, it is possible to analyze the representative matrix of the FBG sensor. This enables understanding what can be expected during the experimental phase, utilizing Panda fibers and birefringence for thermo-mechanical decoupling. The first analysis performed is at a constant ambient temperature of $T_{amb} = 25$ ℃, with strain increasing up to $\varepsilon = 0.05$ (Figure 18 and Figure 19).

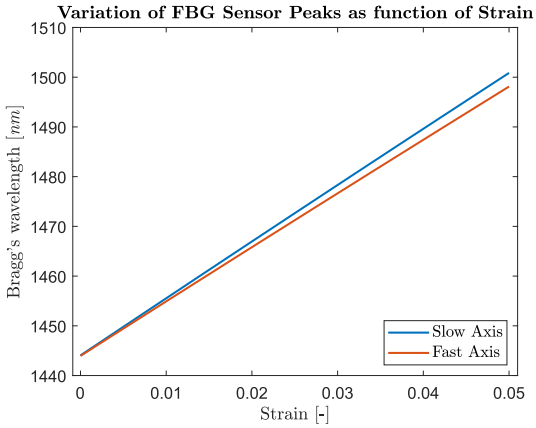

Fig. 18. Change in reflected wavelengths along slow and fast axes during strain variation.

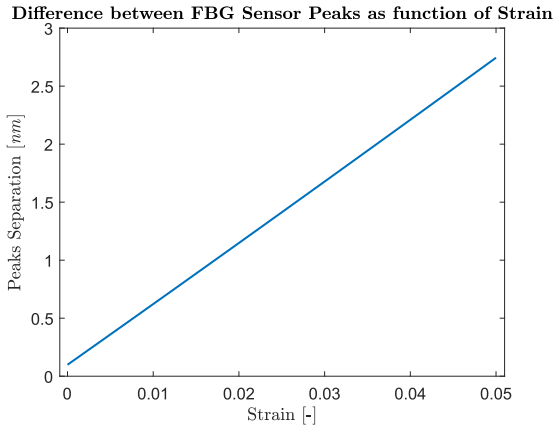

Fig. 19. Difference between slow and fast peak as strain increases.

In Figure 19, the trends of the Bragg wavelength for both the slow and fast axes are reported.

From these curves, it is possible to derive the sensitivity of the two signals to strain. For the slow axis, this sensitivity is $K_{\varepsilon}^{slow} = 1035.3939\ nm/\varepsilon$, while for the fast axis, it is $K_{\varepsilon}^{fast} = 999.0045\ nm/\varepsilon$. From these curves, the sensitivity of the peak separation to strain can also be calculated, which is $K_{\varepsilon}^{d} = 36.3894\ nm/\varepsilon$.

The second analysis performed is with zero deformation while the temperature increases up to $T = 100$ ℃ (Figure 20 and Figure 21).

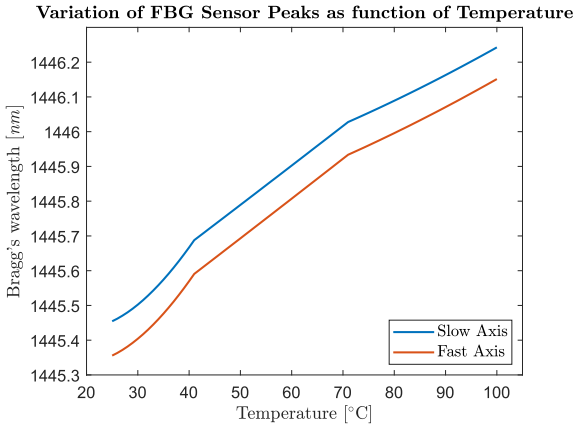

Fig. 20. Change in reflected wavelengths along slow and fast axes during temperature variation.

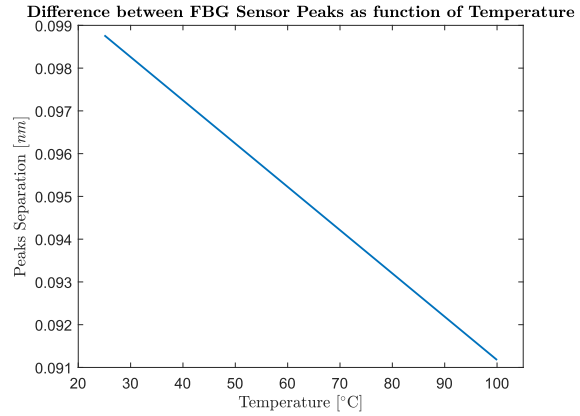

Fig. 21. Difference between slow and fast peak as temperature increases.

From these curves, it is possible to derive the sensitivity of the two signals to temperature variation. For the slow axis, this sensitivity is $K_T^{slow} = 0.0105\ nm/℃$, while for the fast axis, it is $K_T^{fast} = 0.0107\ nm/℃$. From these curves, the sensitivity of the peak separation to temperature can also be calculated, which is $K_T^d = -0.0002\ nm/℃$.

Using the sensitivities obtained from the theoretical model, it is possible to derive the representative matrix of the sensor according to the strategy considered in this work, i.e., tracking the variations in the fast peak and the difference between the two peaks.

$$\begin{pmatrix} \Delta\lambda_{fast} \\ \Delta\, d\lambda \end{pmatrix} = \begin{bmatrix} 0.0107 & 999.0045 \\ -0.0002 & 36.3894 \end{bmatrix} \begin{pmatrix} \Delta T \\ \Delta\varepsilon \end{pmatrix}. \qquad (17)$$

4.2 Experimental results

After performing the numerical calculations, it was found that monitoring the variations in the fast peak and the difference between the two peaks could improve thermo-mechanical decoupling. This approach showed potential for achieving better results compared to previous work. Following this, the experimental activity was initiated.

The birefringent fiber was calibrated using the experimental test bench, which was designed to determine the strain and temperature sensitivity of both signals related to the FBG sensor. The first calibration, for which we report the results, pertains to temperature. The temperature variation range is from -10 ℃ to 140 ℃. We present the values for both the heating and cooling phases (Figure 22 and Figure 23).

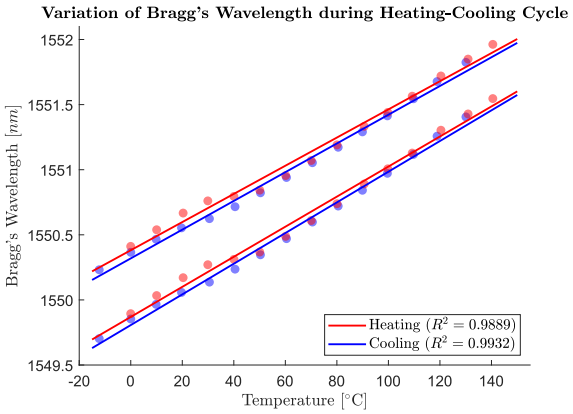

Fig. 22. Change in reflected wavelengths along slow and fast axes for temperature sensitivity calibration during thermal cycle. Experimental values (points) and linear regressions.

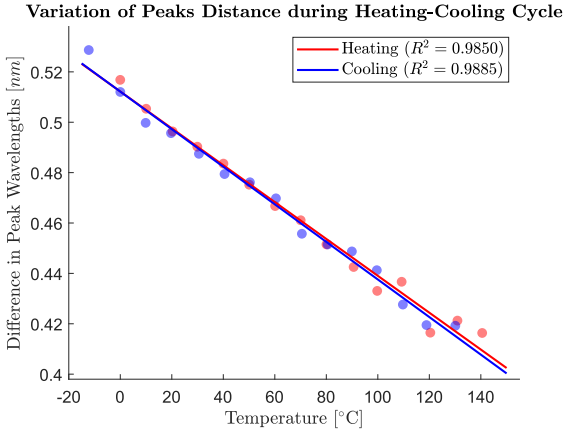

Fig. 23. Variation in wavelength difference during thermal cycle. Evaluation of temperature sensitivity of difference in peak wavelengths. Experimental values (points) and linear regressions.

The strain sensitivity calibration was performed over a range from 0 % to 0.4 %. In this case as well, the results are presented for both the loading and unloading phases (Figure 24 and Figure 25).

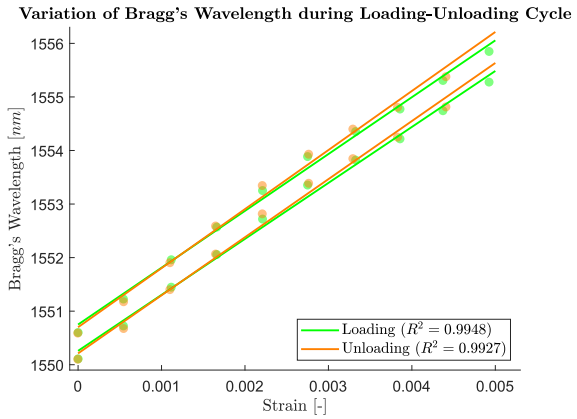

Fig. 24. Change in reflected wavelengths along slow and fast axes for strain sensitivity calibration during loading and unloading cycle. Experimental values (points) and linear regressions.

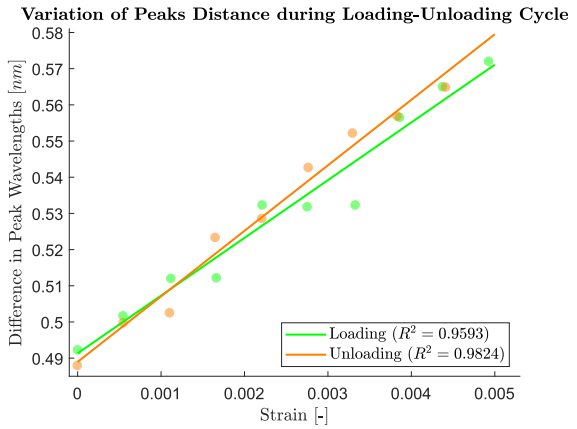

Fig. 25. Variation in wavelength difference during loading and unloading cycle. Evaluation of strain sensitivity of difference in peak wavelengths. Experimental values (points) and linear regressions.

For the calculation of temperature and strain sensitivity coefficients, the average slope of the fitting lines was considered. By using the average slope instead of individual slopes, the variation in sensitivity is less than 2 %, while for the peak difference in the case of strain, it is 5.6 %. These variations are considered small and therefore negligible. The final average sensitivities are summarized in the Table 4.

Table 4. Temperature and strain sensitivity after calibration phase.

K_T^{fast} $[nm/℃]$	0.0117
K_T^{slow} $[nm/℃]$	0.0109
K_T^{d} $[nm/℃]$	-0.0007
K_ε^{fast} $[nm/\varepsilon]$	1064.9215
K_ε^{slow} $[nm/\varepsilon]$	1081.9534
K_ε^{d} $[nm/\varepsilon]$	17.032

The calculated sensitivities were used in mixed deformation and temperature tests. This enabled solving the system of two equations with two unknowns, thereby determining the temperature and strain variations (Figure 26). The initial wavelengths of the two peaks at ambient temperature (25.7198 ℃) and zero strain are $\lambda_{fast_0} = 1550.1089\,nm$ and $\lambda_{slow_0} = 1550.6017\,nm$. The mixed tests include:

- Tests at constant temperature (70 ℃) with strain varying from 0 % to 0.2 %.
- Tests at constant temperature (-5 ℃) with strain varying from 0 % to 0.2 %.
- Tests at constant strain (0.2 %) with temperature varying from 30 ℃ to 96 ℃.
- Tests at constant strain (0.1 %) with temperature varying from -3 ℃ to 22 ℃.

The resolution matrix of the considered linear system includes the sensitivities of the fast axis and those of the peak difference:

$$\begin{pmatrix}\Delta\lambda_{fast}\\ \Delta\, d\lambda\end{pmatrix} = \begin{bmatrix}0.0117 & 1064.9215\\ -0.0007 & 17.032\end{bmatrix}\begin{pmatrix}\Delta T\\ \Delta\varepsilon\end{pmatrix}. \qquad (18)$$

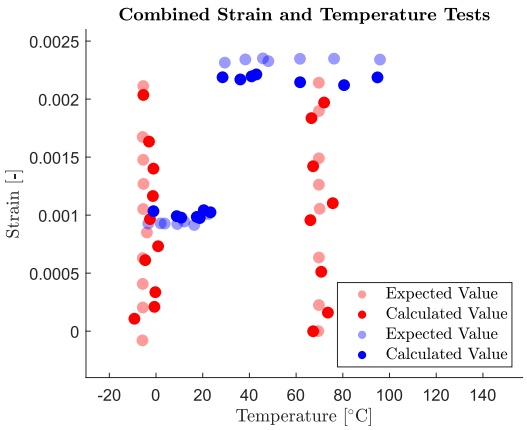

Fig. 26. Mixed temperature and strain tests, difference between expected results and calculated results using sensitivity coefficients.

5. Discussion

The developed analytical model supported the assessment of the feasibility of the strategy used to solve the linear system related to the birefringent FBG sensor. The employed equations facilitated the understanding of the variation in the fundamental parameters governing the behavior of birefringent optical fibers. Theoretical sensitivity coefficients for the slow peak, the fast peak, and the peak difference were calculated. This enabled the evaluation of the most effective pair of equations for determining temperature and strain variations. The three cases are detailed below.

$$\begin{pmatrix}\Delta\lambda_{fast}\\ \Delta\lambda_{slow}\end{pmatrix} = \begin{bmatrix}0.0107 & 999.0045\\ 0.0105 & 1035.3939\end{bmatrix}\begin{pmatrix}\Delta T\\ \Delta\varepsilon\end{pmatrix}. \quad (19)$$

$$\begin{pmatrix}\Delta\lambda_{slow}\\ \Delta\, d\lambda\end{pmatrix} = \begin{bmatrix}0.0105 & 1035.3939\\ -0.0002 & 36.3894\end{bmatrix}\begin{pmatrix}\Delta T\\ \Delta\varepsilon\end{pmatrix}. \quad (20)$$

$$\begin{pmatrix}\Delta\lambda_{fast}\\ \Delta\, d\lambda\end{pmatrix} = \begin{bmatrix}0.0107 & 999.0045\\ -0.0002 & 36.3894\end{bmatrix}\begin{pmatrix}\Delta T\\ \Delta\varepsilon\end{pmatrix}. \quad (21)$$

To determine the effectiveness of this approach for temperature and strain discrimination, the normalized parameter E_d has been introduced [5]. It quantifies how the effects of strain and temperature are uncoupled:

$$\begin{pmatrix}S_1\\ S_2\end{pmatrix} = \begin{bmatrix}c & d\\ e & f\end{bmatrix}\begin{pmatrix}T\\ \varepsilon\end{pmatrix} \quad (22)$$

$$D = cf - de \neq 0 \quad (23)$$

$$E_d = \frac{|D|}{\sqrt{(c^2+e^2)(d^2+f^2)}} \quad (24)$$

E is expressed from 0 to 1, with 1 being the best temperature–strain discrimination and 0 the worst. For the three theoretical systems considered, the obtained values are reported in the Table 5.

Table 5. Determinant D and parameter E_d for three theoretical cases considered: Case 1, fast peak and slow peak; Case 2, slow peak and peak difference; Case 3, fast peak and peak difference.

	$D\ [nm^2/℃\ \varepsilon]$	E_d [%]
Case 1	0.605	2.80
Case 2	0.605	5.56
Case 3	0.605	5.64

As can be seen, the best strategy appears to be the one considered in this article, namely tracking the variations of the fast peak and the difference between the two peaks. The determinant does not change because the second equation is a linear combination of the first with the one related to the slow peak. However, the parameter E_d is significantly higher, indicating the effectiveness of this strategy for mechanical-thermal decoupling.

The same considerations were applied using the sensitivities experimentally obtained from the test bench.

$$\begin{pmatrix}\Delta\lambda_{fast}\\ \Delta\lambda_{slow}\end{pmatrix} = \begin{bmatrix}0.0117 & 1064.9215\\ 0.0109 & 1081.9534\end{bmatrix}\begin{pmatrix}\Delta T\\ \Delta\varepsilon\end{pmatrix}. \quad (25)$$

$$\begin{pmatrix}\Delta\lambda_{slow}\\ \Delta\, d\lambda\end{pmatrix} = \begin{bmatrix}0.0109 & 1081.9534\\ -0.0007 & 17.032\end{bmatrix}\begin{pmatrix}\Delta T\\ \Delta\varepsilon\end{pmatrix}. \quad (26)$$

$$\begin{pmatrix}\Delta\lambda_{fast}\\ \Delta\, d\lambda\end{pmatrix} = \begin{bmatrix}0.0117 & 1064.9215\\ -0.0007 & 17.032\end{bmatrix}\begin{pmatrix}\Delta T\\ \Delta\varepsilon\end{pmatrix}. \quad (27)$$

In addition to parameter E_d, the condition number K of the matrix was also calculated. It measures how sensitive the solution of a system of linear equations is to perturbations in the matrix or in the input values.

Table 6. Determinant D, parameter E_d and condition number K for three cases considered: Case 1, fast peak and slow peak; Case 2, slow peak and peak difference; Case 3, fast peak and peak difference.

	$D\ [nm^2/℃\ \varepsilon]$	E_d [%]	K
Case 1	0.9854	4.06	2338835
Case 2	0.9854	8.32	1188266
Case 3	0.9854	7.92	1151158

Based on the results presented in Table 6, it is preferable to solve a system similar to Case 2 rather than Case 3. Considering the mean and standard deviation of the residuals, i.e., the difference between the actual temperatures and strains and those calculated using the FBG sensor, it is possible to define the performance of the measurement system in terms of accuracy and precision.

Tracking the fast peak and the difference between the two peaks, the measurement system performance is -1.65 ± 3.1 ℃ for temperature and $58.28 \pm 56.2\ \mu\varepsilon$ for strain. In contrast, tracking the slow peak and the difference between the two peaks yields a performance of -1.38 ± 3.18 ℃ for temperature and $69.91 \pm 56.3\ \mu\varepsilon$ for strain.

Figure 26 demonstrates how the accuracy and precision of the measurements, obtained by solving the linear system, decrease as the strain or temperature increases.

The calculation strategies (Case 2 and Case 3) are very similar. The parameter E_d is slightly higher for Case 2, but the conditioning number is lower for Case 3, although the difference is not significant. It is important to emphasize that K is the most critical parameter to consider. The accuracy in temperature measurement is high for both strategies, while for strain measurement, Case 3 performs better. For experimental use, Case 3 is recommended. This is because K is the fundamental parameter for studying the propagation of errors in linear systems, and because strain accuracy is more critical than that of temperature. Therefore, exploiting the variation in the fast peak and the variation in the difference between the two peaks proves to be the best strategy for achieving thermo-mechanical decoupling.

6. Conclusions

In this work, the behavior of birefringent fibers was studied. These enable the achievement of thermo-mechanical decoupling of local measurements using a single Fiber Bragg Grating (FBG) sensor inscribed in the

fiber. The uniqueness of this medium, in which light propagates, lies in its ability to split light along two main polarization axes. This results in two reflected signals from the same sensor at different wavelengths, each responding differently to thermal and mechanical stimuli. This study builds on previous work that explored the feasibility of achieving decoupling using this technology.

In the previous work, a test bench was developed that enabled the testing of birefringent fibers. This setup encountered issues with certain components and the applicable thermal and mechanical stimuli. During this study, the test bench was modified, eliminating hysteresis problems in force and deformation measurements. The temperature range applied to the sensor in the thermal chamber was extended, exceeding $100\ ℃$ and dropping as low as $-10\ ℃$. Additionally, the mechanical clamping system was made more secure to prevent fiber breakage near the chucks. Overall, the test bench was made more reliable and safer for temperature and strain measurements.

The fibers used in this study, as well as the previous one, are Panda fibers. Various strategies were proposed for solving the linear system that provides strain and temperature measurements: tracking the fast and slow peaks, tracking the slow peak and the difference between peaks and tracking the fast peak and the difference between peaks. Before setting up the test bench, the possible behavior of the signals (slow and fast) was studied, proposing a model with six equations based on formulas and parameters from the literature.

The final results show that the parameter E_d, which quantifies how the effects of strain and temperature are uncoupled, is higher when following the strategy of tracking the fast axis and the difference between the two peaks. Although the models employed are simple and rely on significant assumptions, they still provide a rough initial indication of the resolution strategy to be employed. Furthermore, they offer insights into the phenomena governing the behavior of polarization-maintaining (PM) fibers.

The fibers were then tested using the modified test bench, and both thermal and mechanical calibrations were performed. Sensitivity coefficients were used during mixed tests to evaluate sensor performance and strategies in terms of accuracy and precision. The strategy of tracking the fast peak and the difference between the peaks proved to be the most effective, providing temperature and strain values with errors of $-1.65 \pm 3.1\ ℃$ and $58.28 \pm 56.2\ \mu\varepsilon$. All three strategies showed a decrease in accuracy and precision as strain or temperature increased (i.e., as they moved away from the reference condition of room temperature and zero strain).

In the future, the numerical model will be improved to make it more accurate and reliable. The number of fibers tested will also be increased to provide statistical validity to the data obtained in this work. Additionally, a model that considers cross-sensitivity will be implemented to further enhance the accuracy and precision of the measurements. Lastly, birefringent fibers will be embedded in composite material components to assess sensor sensitivity variations and changes in sensor behavior based on the orientation of the fiber section in the composite. The measurement system performance could vary by orienting the polarization axes differently relative to the reinforcing fibers. Therefore, a solution is being studied to embed optical fibers in composites without damaging them or altering their behavior and sensitivity. This strategy would enable the positioning of the fibers along a custom complex path.

These two research efforts could eventually merge to create a simple and compact temperature and strain sensor. This sensor would be easy to install and adaptable to complex paths, meeting users' needs.

Acknowledgements

We extend our sincere gratitude to Diego Henriquet for his commitment and dedication.

This research has been supported by ASI (Italian Space Agency), grant agreement 2018-5-HH.0.

References

[1] S. T. Oh *et al.*, “Discrimination of temperature and strain with a single FBG based on the birefringence effect”, Optics Express, Vol. 12 (2004), No. 4.

[2] D. W. Jung, I. B. Kwon, and N. S. Choi, “Application of a Temperature-Compensating FBG Sensor to Strain Measurement”, Advanced Materials Research, vol. 26–28 (2007), pp. 1089–1092.

[3] Z. Zhou and J. Ou, “Techniques of temperature compensation for FBG strain sensors used in long-term structural monitoring”, Fundamental Problems of Optoelectronics and Microelectronics II, Vol. 5851 (2005), pp. 167–172.

[4] E. Marin and Y. Ouerdane, “Dual-Fibre Bragg Grating Sensor for Simultaneous Temperature and Strain Sensing of Composite Materials Manufacturing”, 7th European Workshop on Structural Health Monitoring, Nantes, France, 2014, 8-11 July, HAL, 9 July 2014.

[5] S. Triollet, L. Robert, E. Marin, and Y. Ouerdane, “Discriminated measures of strain and temperature in metallic specimen with embedded superimposed long and short fibre Bragg gratings”, Measurement Science and Technology, Vol. 22 (2011), No. 1.

[6] Y. J. Rao *et al.*, “Simultaneous strain and temperature measurement of advanced 3-D

braided composite materials using an improved EFPI/FBG system", Optics and Lasers in Engineering, Vol. 38 (2002), pp. 557–566.

[7] S.W. James; M.L. Dockney; R.P. Tatam, "Simultaneous independent temperature and strain measurement using in-fibre Bragg grating sensors", Electronics Letters, Vol. 32 (1996), No. 12, pp. 1133–1134.

[8] C. Femandez-Valdivielso, I. R. Matias, and F. J. Arregui, "Simultaneous Measurement of Strain and Temperature using a Fiber Bragg Grating and a Thermochromic Material", Sensors and Actuators A, Vol. 101 (2002), pp. 107–116.

[9] H. H. Qazi, A. B. Mohammad, H. Ahmad, and M. Z. Zulkifli, "D-shaped polarization maintaining fiber sensor for strain and temperature monitoring", Sensors, Vol. 16 (2016), No. 9.

[10] G. Pereira, M. McGugan, and L. P. Mikkelsen, "Method for independent strain and temperature measurement in polymeric tensile test specimen using embedded FBG sensors", Polymer Testing, Vol. 50 (2016), pp. 125–134.

[11] A. K. Singh, S. Berggren, Y. Zhu, M. Han, and H. Huang, "Simultaneous strain and temperature measurement using a single fiber Bragg grating embedded in a composite laminate", Smart Materials and Structures, Vol. 26 (2017), No. 11, pp. 115025.

[12] G. Sun, H. Tang, Y. Hu, and Y. Zhou, "Strain and temperature discrimination using high birefringence fiber Sagnac interferometer with enhanced sensitivities", IEEE Photonics Technology Letters, Vol. 24 (2012), No. 7, pp. 587–589.

[13] D. P. Zhou, L. Wei, W. K. Liu, and J. W. Y. Lit, "Simultaneous measurement of strain and temperature based on a fiber Bragg grating combined with a high-birefringence fiber loop mirror", Optics Communications, Vol. 281 (2008), No. 18, pp. 4640–4643.

[14] L. A. Ferreira, F. M. Araú, J. L. Santos, and F. Farahi, "Simultaneous measurement of strain and temperature using interferometrically interrogated fiber Bragg grating sensors", Optical Engineering, Vol. 39 (2000), p. 2234.

[15] L. Zhang *et al.*, "Long-distance distributed pressure sensing based on frequency-scanned phase-sensitive optical time-domain reflectometry", Optics Express, Vol. 29 (2021), No. 13, p. 20487.

[16] A. Annunziato, F. Anelli, J. Gates, C. Holmes, and F. Prudenzano, "Design of Polarization-Maintaining FBGs Using Polyimide Films to Improve Strain-Temperature Sensing in CFRP Laminates", IEEE Photonics Journal, Vol. 13 (2021), No. 2, p. 7100315.

[17] J. Van Roosbroeck, S. K. Ibrahim, E. Lindner, K. Schuster, and J. Vlekken, "Stretching the limits for the decoupling of strain and temperature with FBG based sensors", 24th International Conference on Optical Fibre Sensors, Curitiba, Brazil, 2015, SPIE, Vol. 9634 (2015), p. 96343S.

[18] E. Casciaro, D. Rigamonti, and P. Bettini, "Birefringent optical fibers to decouple thermo-mechanical effects on FBG sensors", 11th European Workshop on Structural Health Monitoring, Potsdam, Germany, 11-13 June 2024, eJNDT, Vol. 29 (2024).

[19] A. R. Becker, Introduction to theoretical mechanics, New York, 1954, pp. 45-47.

[20] C. Z. Tan and J. Arndt, "Temperature dependence of refractive index of glassy SiO_2 in the infrared wavelength range", Journal of Physics and Chemistry of Solids, Vol. 61 (2000), pp. 1315-1320.

[21] J. F. Nye, Physical Properties of Crystals: Their Representation by Tensors and Matrices, Oxford science publications, New York, 1985.

[22] K.-H. Tsai, K.-S. Kim, and T. F. Morse, "General Solutions for Stress-Induced Polarization in Optical Fibers", Journal of lightwave technology, Vol. 9 (1991), No. 1.

[23] P. Drexler and P. Fial, "Optical Fiber Birefringence Effects – Sources, Utilization and Methods of Suppression", in: Moh Yasin, Sulaiman W. Harun and Hamzah Arof, Recent Progress in Optical Fiber Research, IntechOpen, chapter 7, 2012.

[24] C. Caucheteur, T. Guo, and J. Albert, "Polarization-Assisted Fiber Bragg Grating Sensors: Tutorial and Review", Journal of Lightwave Technology, Vol. 35 (2017), No. 16, pp. 3311–3322.

[25] D. Donadio, M. Bernasconi, and F. Tassone, "Photoelasticity of sodium silicate glass from first principles", Physical Review B, Vol. 70 (2004), No. 21, pp. 1–9.

[26] K. E. Cramer, M. Hayward, and W. T. Yost, "Quantification of Residual Stress from Photonic Signatures of Fused Silica", 40th Annual Review of Progress in Quantitative Nondestructive Evaluation, Baltimore, Maryland, USA, 21-26 July, 2013, AIP Conference Proceedings, Vol. 1581 (2014), No. 1, pp. 1679-1686.

[27] R. Guan, F. Zhu, Z. Gan, D. Huang, and S. Liu, "Stress birefringence analysis of polarization maintaining optical fibers", Optical Fiber Technology, Vol. 11 (2005), No. 3, pp. 240–254.